Carrier dynamics in bulk ZnO. II. Transient photoconductivity measured by time-resolved terahertz spectroscopy

Jason B. Baxter[1,*,†] and Charles A. Schmuttenmaer[2,*,‡]
[1]*Department of Chemical and Biological Engineering, Drexel University, 3141 Chestnut Street, Philadelphia, Pennsylvania 19083, USA*
[2]*Chemistry Department, Yale University, P.O. Box 208107, 225 Prospect Street, New Haven, Connecticut 06520, USA*
(Received 12 August 2009; revised manuscript received 25 November 2009; published 30 December 2009)

We employ time-resolved terahertz spectroscopy to investigate the dynamics of photogenerated electrons and holes in bulk ZnO at temperatures below 100 K. Carrier density and mobility are extracted by fitting the Drude model to the measured frequency-dependent complex photoconductivity. Electrons are excited with below-band-gap photons (387, 400, or 775 nm) to states well above the conduction-band minimum by one-photon absorption from midgap states. Two-photon absorption also occurs with blue excitation, leading to the generation of mobile valence-band holes as well as electrons. Within a few picoseconds of excitation with blue photons, carriers have ambipolar scattering times of over 500 fs, corresponding to combined carrier mobility of $\sim 3500\ \mathrm{cm^2\ V^{-1}\ s^{-1}}$. Scattering times decrease to ~300 fs as the light holes relax to the heavy-hole bands over the next tens to hundreds of picoseconds. Higher temperatures and higher excitation fluences result in faster relaxation, as well as faster recombination, due to increased carrier interaction with phonons and other carriers. Carrier lifetimes at low excitation fluences with blue photons range from 20 ps at 80 K to nearly 200 ps below 40 K. Conversely, photoexcitation with red photons produces dynamics that are independent of fluence, which is likely due the lack of mobile holes compared to blue excitation.

DOI: 10.1103/PhysRevB.80.235206 PACS number(s): 72.20.Jv, 72.40.+w, 78.20.−e, 78.47.J−

I. INTRODUCTION

ZnO is a wide band-gap semiconductor (E_g=3.37 eV) with large exciton binding energy (60 meV), enabling its use in diverse applications as a light emitter,[1,2] transparent-conducting oxide,[3] transparent thin-film transistor,[4] and electron-transport material in nanostructured solar cells.[5–7] Electron-hole and exciton dynamics are central to each of these applications, and developing a detailed understanding of charge-carrier creation, cooling, exciton formation, trapping, and recombination is critical to improving their performance.

Carrier dynamics in ZnO bulk crystals, thin films, nanowires, and nanoparticles can be investigated by introducing electrons into the conduction band by doping, by direct photoexcitation of the ZnO, by interfacial electron transfer from an adsorbed sensitizer, by thermal excitation, or by an electron beam. The electron density and initial excess energy above the conduction-band minimum as well as sample temperature, defect structure, and morphology all affect dynamics of carrier transport, recombination, and exciton formation. The photoexcited carrier population decays by exciton formation and radiative recombination as well as by nonradiative recombination at defect sites. Recent evidence has shown that excitons are formed on time scales of ~1–100 ps, after carriers have cooled independently through the electron-hole continuum.[8]

Characterizing ZnO hole mobilities and dynamics has been challenging due to difficulty in growing *p*-type ZnO. Undoped ZnO is typically *n* type with intrinsic donor densities an order of magnitude larger than acceptor densities,[9] but optical excitation can be used to generate both electrons and holes in equal numbers. In many semiconductors, holes have a much larger effective mass than electrons and therefore play only a minor role in conductivity. However, in ZnO, it is possible to generate holes that are as light as electrons when exciting from the appropriate valence band (VB).[10] While symmetry does not allow the optical transition from the light-hole valence band to the lowest-lying conduction band for single-photon excitation, this transition is allowed in the case of a two-photon absorption process.

Carrier population and mobility can both be monitored using time-resolved terahertz spectroscopy (TRTS). TRTS uses an optical pump to photogenerate conduction-band electrons and valence-band holes in a semiconductor followed by a terahertz (THz) probe to measure their conductivity. TRTS is an ideal method to measure electrical properties of semiconductors because it is noncontact, its frequency range brackets typical carrier scattering rates which allows detailed modeling, and dynamics can be measured with subpicosecond time resolution. The THz radiation is attenuated and dispersed by intraband transitions in proportion to the conductivity. Instantaneous carrier density and mobility can be derived from the measured complex photoconductivity by application of appropriate models. The Schmuttenmaer group has previously employed TRTS to measure transient photoconductivity in GaAs wafers[11] and thin films[12] as well as ZnO nanowires, nanoparticles, and thin films.[13] Other workers have used TRTS to investigate carrier dynamics arising from two-photon absorption in bulk CdTe and ZnTe,[14] exciton formation in ZnO wafers,[8] transient conductivity in nanoporous InP membranes,[15] transient conductivity in GaAs and InGaAs nanowires,[16,17] and transient conductivity in gold films with thickness between 2 and 28 nm.[18]

In this paper, we report on the dynamics of carrier density and mobility in photoexcited bulk ZnO as a function of excitation wavelength, excitation fluence, and wafer temperature. Frequency-dependent, complex photoconductivity was measured by TRTS, and plasma frequency and scattering time were extracted by fitting with the Drude model. Mobile

electrons were generated by one-photon absorption and electron-hole pairs were generated via two-photon absorption. The relative magnitude of these two modes of excitation depends on excitation wavelength and fluence. In all cases, both carrier density and mobility, which are calculated from the Drude fitting parameters, reach their maximum values within the first ~5 ps of photoexcitation and decay slowly over tens to hundreds of picoseconds. Initial combined carrier mobilities are up to 3500 $cm^2\ V^{-1}\ s^{-1}$ and fall to ~2000 $cm^2\ V^{-1}\ s^{-1}$ within 200 ps as light-holes cool into heavy-hole bands. After relaxation, these mobilities are comparable to what we have previously measured at similar temperatures for carriers thermally excited to the conduction-band minimum.[19] Interaction with other carriers plays a critical role in relaxation dynamics and the photoconductivity decays faster with increasing carrier density, where additional carriers can be generated by either higher excitation fluence or higher temperature.

II. EXPERIMENTAL METHODS

The ZnO wafer studied was 10 mm × 10 mm, 380 μm thick, and (0001) cut. It was grown from the melt by Cermet, Inc. and is nominally undoped but displays *n*-type conductivity. We estimate room-temperature electron densities of 5×10^{16} cm^{-3} from THz time-domain spectroscopy.[19] It was mounted over a 6 mm aperture in a brass holder with an identical neighboring 6 mm aperture to allow for reference measurements. The holder was mounted in a helium cryostat to allow measurements to below 10 K.

An amplified Ti:Sapphire laser (Spectra Physics Tsunami/Spitfire) was used to generate 800 mW of pulsed near-IR light at 1 kHz repetition rate. The pulse width was ~100 fs and the center wavelength could be varied from 775 to 820 nm. About 2/3 of the power was frequency doubled to produce up to 120 mW of blue or near-UV light for the pump beam. A series of four parabolic mirrors focuses the THz radiation to a spot size of ~3 mm at the sample and then onto a second ZnTe(110) crystal for detection by free-space electro-optic sampling. Details on the TRTS spectrometer have been published previously.[11] Since higher THz frequencies are more tightly focused at the sample, care was taken to ensure that the pump beam-spot size (~8 mm) was significantly larger than the THz spot size (~3 mm) for frequency-dependent studies.

The frequency-dependent, complex permittivity of the ZnO was determined by Fourier transforming the THz time-domain scans with and without the ZnO wafer in the beam path. Details of the data analysis have been reported previously.[13,20] Permittivity of the photoexcited sample was determined by measuring the difference between the photoexcited and nonphotoexcited sample in the time domain and adding it to the nonphotoexcited ZnO scan to create a photoexcited waveform. Because the difference in signal intensity between photoexcited and nonphotoexcited samples is an order of magnitude smaller than the signal itself, this difference method allows much more accurate determination of the photoconductivity than taking successive scans with and without photoexcitation. Less than half of the pump beam power was absorbed by the ZnO so our calculations assume that the photoexcited carriers are generated essentially uniformly throughout the wafer thickness. The calculated conductivities represent the average response of all photoexcited charges. When exciting out of midgap states, we assume that the response is primarily due to electrons since the holes left behind have very high effective mass. However, when exciting from the valence band to the conduction band via two-photon absorption, electrons and holes have similar effective masses and both will contribute to the THz absorption.[10]

The THz response was measured at a series of delay times after photoexcitation under various excitation conditions. The frequency-dependent, complex-valued photoconductivity, $\hat{\sigma}$, is obtained from

$$\hat{\eta}(\omega) = \hat{\varepsilon}(\omega) + \frac{i\hat{\sigma}(\omega)}{\varepsilon_0 \omega}, \tag{1}$$

where $\hat{\eta}$ is the photoexcited permittivity, $\hat{\varepsilon}$ is the nonphotoexcited permittivity, ω is the angular frequency, ε_o is the free-space permittivity, and i is the unit imaginary. We emphasize that this photoconductivity is the *change* in conductivity upon photoexcitation and not the overall conductivity.

Pump scans were performed by measuring the transmission change at the time-domain peak of the THz waveform as a function of pump-probe delay time.[11] All THz frequencies are in phase at the peak so the pump scans represent the average far-infrared (far-IR) response of the sample. Pump scans were performed as a function of temperature, excitation wavelength, and excitation fluence.

III. RESULTS AND DISCUSSION

A. One- and two-photon absorption in ZnO

We have investigated photoconductivity resulting from near-UV (387 nm), blue (400 nm), and red (775 nm) excitation. The low-temperature band gap of ZnO, 3.37 eV or 368 nm, is just beyond the tunable range of the frequency-doubled Ti:Sapphire pulse. Consequently, the majority of electrons excited into the conduction band are from midgap states or are the result of two-photon absorption (TPA). It is also possible for photoexcitation to promote electrons from the band tail of the ZnO, particularly with near-UV excitation at higher temperatures. Figure 1(a) shows the temperature-dependent optical transmission for pump wavelengths of 387 and 400 nm. The room temperature UV-visible transmission spectrum of the ZnO wafer is shown as an inset in Fig. 1(b). Measurements were made in transmission and do not account for reflection. Adjusting for reflection would slightly shift the absorption curves but would not alter their shape significantly. The band gap widens at low temperature, resulting in an increased fraction of transmitted 387 nm photons as the band gap becomes larger than the photon energy. At 400 nm, the fraction transmitted is independent of temperature and we therefore conclude that no direct above-band-gap excitation is possible with this photon energy at or below room temperature. The fraction of absorbed photons is less than 40% and is constant for both wavelengths at temperatures below 200 K, indicating excitation from midgap states and TPA.

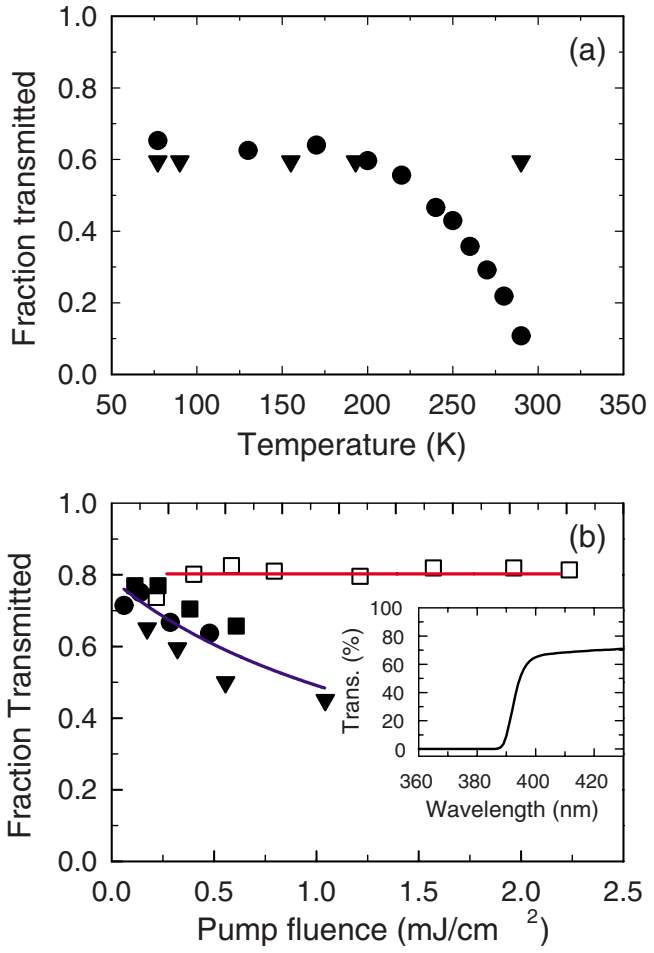

FIG. 1. (Color online) Fraction of photons transmitted as a function of (a) substrate temperature with 0.4 mJ/cm^2 laser fluence and (b) laser fluence at substrate temperature of 77 K. Photon wavelengths are 387 nm (solid circles), 400 nm (solid triangles), 410 nm (solid squares), and 775 nm (open squares). Inset in (b) is a room-temperature UV-visible transmission spectrum of the ZnO wafer. Curves are fits of the transmitted power as described in the text, where all three blue wavelengths are grouped together.

To determine if absorption is occurring from midgap states or from a multiphoton process, we measured the fraction of pump light transmitted as a function of incident pump power for four different pump wavelengths at 77 K as shown in Fig. 1(b). Approximately 20% of 775 nm photons are either reflected or absorbed. Calculating reflectivity from the refractive index indicates that nearly all of this 20% is reflected with only a small fraction absorbed. Transmission of 775 nm light is independent of incident pump fluence, indicating that each absorbed photon excites an electron from a midgap state into the conduction band.

When exciting with low power at 387, 400, and 410 nm, approximately 25% of photons are reflected or absorbed at 77 K. The percent reflection near the band edge is likely to be 10–20 % (Ref. 21) but was not measured directly. The remaining ~10% of photons are absorbed. The absorbed fractions of these three wavelengths are very similar because all are below the low-temperature band gap as seen in Fig. 1(a). The absorbed fraction of the near-UV excitation is significantly higher than that of the red excitation. This difference results because the blue photon energy is sufficient to excite from midgap states throughout most of the band gap while red photons can only excite from states in the upper half of the band gap and more importantly because blue photons can be absorbed by two-photon processes. The photoexcited electrons generated from blue/near-UV excitation are likely to have initial energy 1–3 eV above the conduction-band minimum while those generated from red excitation can have no more than 1.6 eV excess energy and are likely to have much less.

Two 775 nm photons do not have enough energy to excite an electron above the band gap by TPA, which explains why there is no variation in absorption with incident power. In one-photon absorption (OPA), the transmitted intensity I through a distance l is directly proportional to the incident intensity I_0: $I=TI_0$, where $T=e^{-\alpha l}$ (α is the absorption coefficient). Therefore, the fractional power transmitted is $P/P_0=T$ since power is simply intensity multiplied by area. If the material undergoes TPA, then $I=I_0/(1+I_0\beta l)$, where β is the two-photon absorption coefficient. If both OPA and TPA are occurring then $I=TI_0/(1+I_0\beta l)$ and $P/P_0=T/(1+I_0\beta l)$. The lines in Fig. 1(b) are fits of the latter function to the transmission data. Due to scatter in the measured fractional transmission, the data using 387, 400, and 410 nm excitation were grouped together. For 775 nm excitation, we find that $T=0.80$ and $\beta=0.0$, confirming that TPA does not occur at this wavelength. For blue excitation wavelengths, $T=0.79$ and $\beta=6.9$ cm/GW. In all cases optical transmission is greater than 40%, indicating penetration depths of at least the 380 μm thickness of the wafer. This transmissivity is consistent with room-temperature UV-visible transmission of this wafer, as shown in the inset to Fig. 1(b), when corrected for the ~7 nm shift in absorption edge at low temperature. Therefore, in our photoconductivity calculations we assume that carriers are generated uniformly throughout the full wafer thickness. These calculations yield average carrier properties and do not account for distributions of carriers within the wafer which result from different absorption processes.

B. Transient photoconductivity in ZnO with 387 nm excitation at 10 K

Transient photoconductivity was probed using THz radiation after optical photoexcitation. Figure 2 shows the real and imaginary photoconductivity of the ZnO wafer from 0.1–1.6 THz at 10 K for a number of pump-probe delay times after excitation with 0.15 mJ/cm^2 fluence of 387 nm photons. The photoconductivity reaches a maximum within the first ~5 ps after photoexcitation, remains fairly constant over the next ~20 ps, and then decreases as the carriers relax on time scales of tens to hundreds of picoseconds. Similar trends and magnitudes for photoconductivity were found using other combinations of wavelength, fluence, and ZnO temperature. The general form of the photoconductivity spectrum is the same as that for intrinsic conductivity of the same wafer[19] but the relative magnitudes differ significantly as a function of temperature and excitation fluence. The maximum real photoconductivity that we observed was 0.05

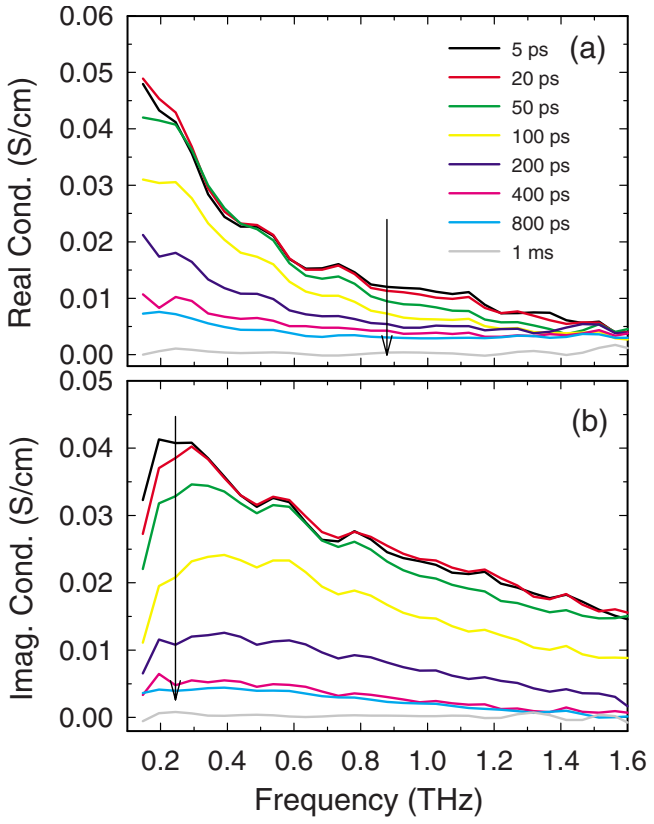

FIG. 2. (Color online) (a) Real and (b) imaginary photoconductivity for a series of pump-probe delay times. ZnO was maintained at 10 K and was photoexcited with 0.15 mJ/cm^2 laser fluence of 387 nm photons. Legend applies to both real and imaginary photoconductivities.

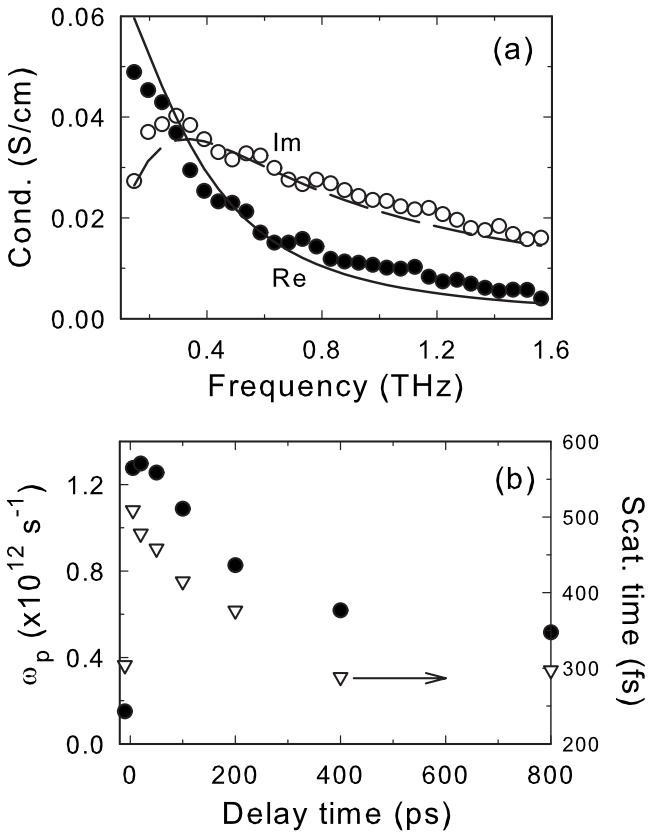

FIG. 3. (a) Fit of the Drude model (lines) to experimental photoconductivity data (points) at 10 K, 20 ps after photoexcitation. (b) Plasma frequency (filled circles) and scattering time (open triangles) as a function of pump-probe delay time. ω_p and τ are extracted by fitting the Drude model to the photoconductivity data in Fig. 2.

S/cm while intrinsic conductivity of the same wafer ranged from 3 S/cm at 120 K to less than 0.01 S/cm below 30 K. The photoconductivity is much smaller than the intrinsic conductivity at higher temperatures because many more electrons are thermally excited from shallow donor states by a temperature change of a few tens of degrees Celsius than are photoexcited with this low fluence of below-band-gap photons. Conversely, photoconductivity dominates intrinsic conductivity at 10 K.

The complex conductivity data are fit well by the Drude model, the most common and straightforward model for conductivity in metals and semiconductors. For example, Fig. 3(a) shows the photoconductivity at 20 ps from Fig. 2 along with the Drude fit to the data. The Drude model considers a free-electron gas with complete momentum randomization following elastic scattering events, dictating that the real component of the conductivity has its maximum value at dc and that the imaginary component is positive with a maximum at the frequency of the carrier-scattering rate. The frequency-dependent conductivity based on the Drude model is given by

$$\hat{\sigma}(\omega) = \frac{\varepsilon_0 \omega_p^2 \tau}{(1 - i\omega\tau)}, \tag{2}$$

where ε_0 is the permittivity of free space, ω_p is the plasma frequency, and τ is the characteristic scattering time.[22] The scattering time represents mobile carriers' average time between collisions. The electron density, N_e, and plasma frequency are related through

$$N_e = \frac{\varepsilon_o \omega_p^2 m^*}{e^2} \tag{3}$$

while the dc mobility, μ, for a Drude conductor is given by

$$\mu = \frac{e\tau}{m^*}, \tag{4}$$

where e is the magnitude of the electron charge and m^* is the carrier effective mass: $\frac{1}{m^*} = \frac{1}{m_e^*} + \frac{1}{m_h^*}$. Near the band edges, the relative effective masses are $0.24m_e$ for electrons,[23] 0.25 for light holes, and 0.48 for heavy holes.[10] However, effective masses may be quite different when carriers are excited to large excess energies.[24] Because of the range of effective masses possible for carriers in this work, we will present results primarily in terms of scattering times and plasma frequencies with occasional reference to carrier densities and mobilities in specific cases.

Plasma frequencies and scattering times were extracted from the far-IR response by fitting the Drude model to the photoconductivity data at each delay time. The evolution of

the best-fit values is shown in Fig. 3(b) for excitation with 387 nm photons and a wafer temperature of 10 K. As expected, the plasma frequency increases sharply just after the arrival of the pump pulse, reaches a maximum of 1.3 $\times 10^{12}$ s^{-1} within 20 ps, and then decays to less than 40% of its maximum level over hundreds of picoseconds as carriers are trapped, recombine, or form excitons. Hendry *et al.*[8] provide evidence for exciton formation by carrier cooling through the electron-hole continuum followed by acoustic phonon emission. However, no excitonic signature was found in our system. The THz response resulting from conductivity of free carriers is much larger than that from polarizability of insulating excitons at the same number density. Even at the longest delay times of over 500 ps, there is still a substantial density of free carriers remaining in our ZnO. The response of these free carriers overwhelms any excitonic signal and inhibits their detection. Longer persistence of free carriers in our ZnO compared to Hendry's may result from different densities and types of defects in the ZnO samples or variations in carrier densities that arise from different excitation conditions.

The maximum scattering time, 510 fs, is seen at the earliest delay time measured, 5 ps, and scattering time decreases monotonically with increasing time after photoexcitation. Electrons are excited well above the conduction-band minimum and one might expect that scattering times would increase as electrons cool to the conduction-band minimum where the band curvature is highest. However, holes produced by TPA must also be considered. TPA selectively generates light holes, which then cool and scatter into the heavy-hole bands over hundreds of picoseconds via carrier-carrier scattering and phonon emission. This transition from light holes to heavy holes leads to lower ambipolar scattering times of ~300 fs. Neglecting the contribution of heavy holes to the free-carrier absorption, electron mobilities of ~2000 $cm^2\ V^{-1}\ s^{-1}$ are seen for long delay times of at least 400 ps. This mobility is similar to that which we have measured for electrons thermally excited to just above the edge of the conduction band from shallow donor states at temperatures of 40–120 K.[19]

C. Physical basis for selective generation of light holes by two-photon absorption

The selective creation of light holes, rather than heavy holes, by TPA can be understood by considering the ZnO band structure and the selection rules for one- and two-photon transitions. The band structure of ZnO is shown in Fig. 4.[25–28] The spin-orbit interaction in ZnO is quite small ($\Delta_{so} \approx -3.5$ mV, compared to 340 mV in GaAs) and can be neglected in this context. In wurtzite, which has C_{6v} symmetry, the conduction band is Γ_1, the highest valence band (VB_A) is Γ_5, and the next-highest valence band (VB_B) is Γ_1.

When polarization is parallel to the optic axis (the z axis or the c axis), referred to as $E \| c$, the dipole operator for optical transitions transforms as $\Gamma_1(z)$. When the polarization is perpendicular to it, referred to as $E \perp c$, the dipole operator transforms as $\Gamma_5(x,y)$.[29] We use the notation of Ref. 30.

One-photon optical transitions are allowed if the direct product of the initial-state symmetry and the symmetry of the transition contains the final-state symmetry.[29] Two-photon optical transitions are allowed if the symmetry of the final state is contained in the product of the initial-state times the transition, times the symmetry of the transition a second time. At the zone center, the symmetry of the conduction band is Γ_1. For one-photon $E \perp c$ transitions

$$VB_A: \Gamma_5^v \otimes \Gamma_5(x,y) = \Gamma_1 \oplus \Gamma_2 \oplus \Gamma_6 \quad \therefore \text{allowed},$$

$$VB_B: \Gamma_1^v \otimes \Gamma_5(x,y) = \Gamma_5 \quad \therefore \text{forbidden}.$$

And for two-photon $E \perp c$ transitions, the opposite holds

$$VB_A: [\Gamma_1 \oplus \Gamma_2 \oplus \Gamma_6] \otimes \Gamma_5(x,y) = \Gamma_5 \oplus \Gamma_5 \oplus \Gamma_3 \oplus \Gamma_4 \oplus \Gamma_5 \quad \therefore \text{forbidden},$$

$$VB_B: \Gamma_5 \otimes \Gamma_5(x,y) = \Gamma_1 \oplus \Gamma_2 \oplus \Gamma_6 \quad \therefore \text{allowed}.$$

When spin-orbit coupling is included, VB_A splits into two bands, which are labeled as VB_A and VB_B, and VB_B becomes VB_C. In ZnO Δ_{so} is negative, so VB_A has symmetry Γ_7 while VB_B has symmetry Γ_9. VB_C has symmetry Γ_7, as does the conduction band. The transition dipole operator still has symmetry $\Gamma_1(z)$ for $E \| c$ and has $\Gamma_5(x,y)$ for $E \perp c$. The transitions from VB_A and VB_B that become allowed when including spin-orbit coupling are only weakly allowed because the spin-orbit coupling is small and they were forbidden prior to including it.[31]

One photon $E \perp c$ transitions

$$VB_A: \Gamma_7^v \otimes \Gamma_5(x,y) = \Gamma_7 \oplus \Gamma_9 \quad \therefore \text{allowed},$$

$$VB_B: \Gamma_9^v \otimes \Gamma_5(x,y) = \Gamma_7 \oplus \Gamma_8 \quad \therefore \text{allowed},$$

$$VB_C: \Gamma_7^v \otimes \Gamma_5(x,y) = \Gamma_7 \oplus \Gamma_9 \quad \therefore \text{weakly allowed}.$$

Two photon $E \perp c$ transitions

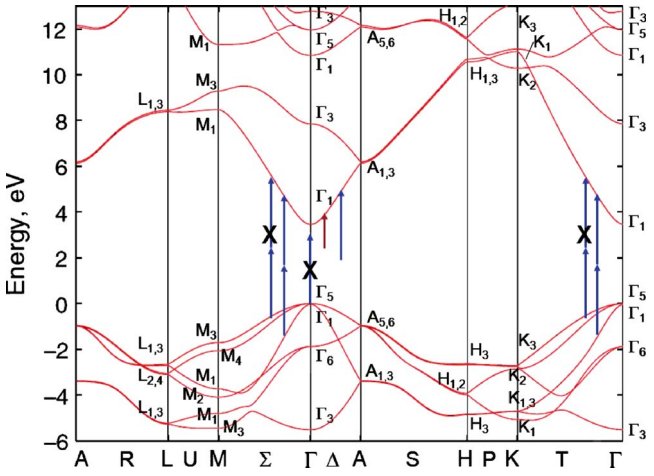

FIG. 4. (Color online) Band diagram of ZnO. Lines schematically show allowed one- and two-photon transitions. Examples of one-photon transitions that are not allowed because photon energies are too small and of two-photon transitions forbidden due to symmetry are shown with an "X." Adapted from Fig. 1 of Ref. 25.

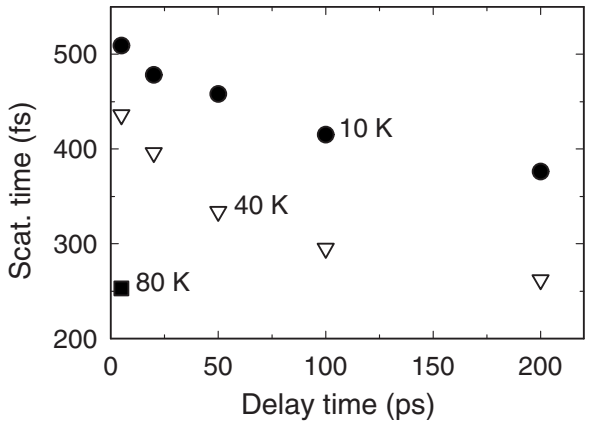

FIG. 5. Scattering time as a function of delay time for ZnO temperatures of 10, 40, and 80 K showing faster carrier relaxation at higher temperatures. Excitation conditions were the same as in Fig. 2.

$$\mathrm{VB}_A\colon [\Gamma_7 \oplus \Gamma_9] \otimes \Gamma_5(x,y) = \Gamma_7 \oplus \Gamma_9 \oplus \Gamma_8 \quad \therefore \text{weakly allowed},$$

$$\mathrm{VB}_B\colon [\Gamma_7 \oplus \Gamma_8] \otimes \Gamma_5(x,y) = \Gamma_7 \oplus \Gamma_9 \oplus \Gamma_8 \quad \therefore \text{weakly allowed},$$

$$\mathrm{VB}_C\colon [\Gamma_7 \oplus \Gamma_9] \otimes \Gamma_5(x,y) = \Gamma_7 \oplus \Gamma_9 \oplus \Gamma_8 \quad \therefore \text{allowed}.$$

Therefore, including spin-orbit coupling has only a minor influence on the observed behavior.

Selective generation of light holes and their subsequent relaxation to heavy-hole bands explains the decrease, rather than increase, in ambipolar scattering time as a function of pump-probe delay time. This effect would not be seen when photoexciting with above-band-gap photons since the transition from the light-hole band is not allowed with one-photon absorption. In many materials, the hole effective mass is much greater than the electron effective mass and conductivity can be attributed exclusively to the electrons. However, as can be seen from the band diagram, this is not the case for ZnO. Therefore, both electrons and holes contribute to the photoconductivity under TPA conditions.

D. Effect of temperature on photoexcited carrier dynamics

Carrier relaxation is faster at higher lattice temperatures since there is increased scattering from phonons as well as from other carriers that have been thermally excited. Figure 5 shows the evolution of the scattering time over the 200 ps following photoexcitation with 387 nm photons at wafer temperatures from 10–80 K. Five ps after photoexcitation, the scattering time is 510 fs at a lattice temperature of 10 K, 440 fs at 40 K, and only 250 fs at 80 K. The 10 and 40 K data decay exponentially to a value of ~280 fs with time constants of 200 and 60 ps, respectively. Carriers are excited to an equally high mobility state at very short times regardless of temperature but the additional carrier-carrier and carrier-phonon scattering at higher temperatures causes holes to relax into the heavy-hole band much more quickly.

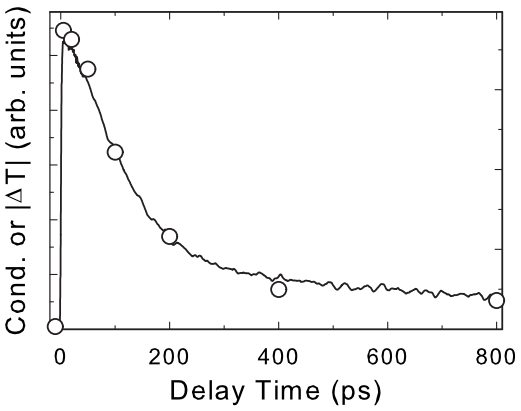

FIG. 6. Normalized photoconductivity from pump scan (line) along with fitted dc conductivity (points). Excitation with 387 nm photons at 0.15 $\mathrm{mJ/cm^2}$ with ZnO temperature of 10 K. The magnitude of ΔT was plotted so that it would be a positive quantity.

Continuous measurements of the transient average far-IR conductivity were made using pump scans[11] to complement the full frequency-dependent conductivity measured at discrete times (shown in Figs. 2, 3, and 5). Figure 6 shows an example pump scan using 387 nm excitation at 10 K along with the fitted dc photoconductivity of the data in Fig. 2 which is proportional to $\omega_p^2\tau$. The change in THz transmission is proportional to the photoconductivity so the pump scan follows the same trend as seen when measuring photoconductivity at discrete points, rising quickly to a maximum after the photoexcitation event and then decaying as the carrier density decreases and the carriers relax to the band edges.

A series of pump scans confirms that relaxation dynamics are much faster at higher ZnO temperatures. Figure 7(a) displays the change in total THz transmission as a function of pump-probe delay time for a series of temperatures ranging from 10–100 K. The pump wavelength was 400 nm and the pump fluence was 0.07 $\mathrm{mJ/cm^2}$. Excitation with 400 nm photons occurs either by TPA or from midgap states as discussed in relation to Fig. 1(a) with resulting electrons having energy several eV above the band edge and light holes with energies several eV below the valence-band maximum. In all cases, the photoconductivity increases rapidly within the first few picoseconds of photoexcitation then decays as carriers cool and recombine. The maximum relative photoinduced change to the nonphotoexcited transmission was ~2% in all cases. However, the absolute magnitude of the transmission change decreases with increasing temperature due to larger background absorption of the THz probe by a large population of thermally generated free carriers.

Since the fraction of light absorbed at a given wavelength is constant over the temperature range considered here, the number of carriers generated by photoexcitation is independent of temperature. Assuming a carrier effective mass of $0.24m_e$ in Eq. (3), the plasma frequencies under these excitation conditions correspond to maximum carrier densities on the order of 1×10^{14} $\mathrm{cm^{-3}}$. Normalizing the pump scans by their maximum transmission change, Fig. 7(b), reveals that photoconductivity decays much faster at higher temperatures. As indicated in Fig. 3(b), the decay in photoconductiv-

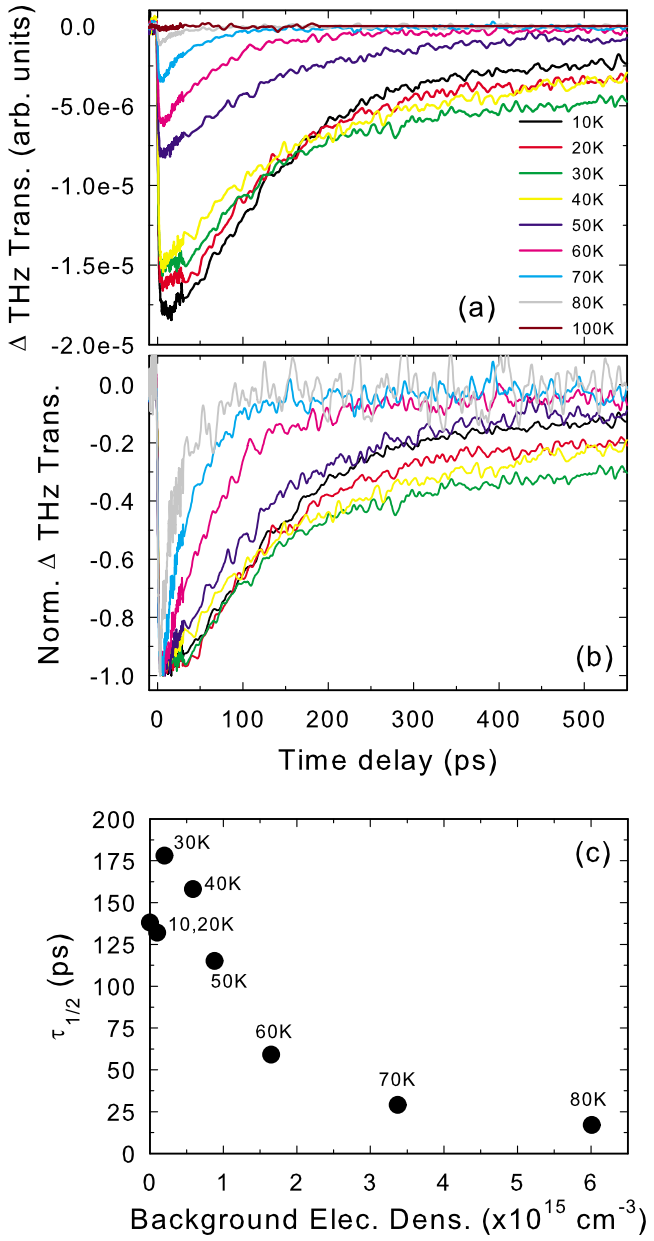

FIG. 7. (Color online) (a) Pump scans with 0.07 mJ/cm^2 fluence of 400 nm photoexcitation as a function of ZnO temperature and (b) same pump scans normalized by their maximum transmission change. Same legend applies to both panels. (c) Time for change in THz transmission due to photoexcited carriers (λ=400 nm) to be reduced to half of its maximum value as a function of background electron density, where background electron density is varied by changing the ZnO temperature. Generally the magnitude of transmission change is smaller and the photoconductivity decays faster at higher temperatures, with the exception of fast decay at 10 and 20 K.

ity is due to decrease in both carrier density and mobility. At high temperature the larger population of thermally excited electrons and holes provide more opportunities for recombination, thereby decreasing the photoexcited carrier population more rapidly. With 0.07 mJ/cm^2 of 400 nm excitation, the photoexcited electron population is much larger than the thermally excited population at 10 K. At 40 K they are approximately equal and at 100 K the thermally excited electron population is more than ten times larger than the photoexcited population. Additionally, carrier-phonon interactions that allow the hot carriers to cool by dissipating energy into the lattice are more prevalent at high temperature where more phonon states are occupied. Faster scattering at high temperatures causes light holes to relax into heavy-hole bands more quickly and the resulting decrease in mobility also contributes to the decay in photoconductivity.

The decay in photoconductivity is nearly, but not quite, exponential. Notably, midrange temperatures (~20–40 K) maintain a nonzero offset for long times (beyond 500 ps). The time to decay to $\Delta T_{max}/2$ is shown as a function of background electron density in Fig. 7(c). Background electron density is excited thermally and was measured by THz time-domain spectroscopy.[19] One reason why the pump scans do not follow simple exponential decay dynamics is that they measure photoconductivity, rather than simply carrier density. Mobility also contributes to photoconductivity and mobility changes over time as demonstrated earlier in the discussion of scattering times. The combination of changing carrier density and mobility gives rise to a crossing of the low-temperature and mid-temperature scans. While the 30 K through 100 K data follow monotonic trends, the 10 and 20 K scans intersect the 30 and 40 K scans around 125 ps. Similar behavior for ZnO can be seen in work by Hendry *et al.*[8] but was not commented upon explicitly. Schall and Jepsen[14] report a delayed minimum in the photoconductivity of CdTe that results from different spatial distributions and cooling rates of electrons that arise from OPA and TPA processes. Given the strong temperature dependence of TPA,[14] this is the likely explanation in our case as well.

E. Effect of excitation fluence and wavelength on carrier dynamics

In addition to temperature, dynamics also depend on excitation fluence and wavelength. The power dependence of the carrier density, assuming a carrier effective mass of $0.24m_e$, was measured at each excitation wavelength, as shown in Fig. 8. There is an approximately linear relationship between incident pump fluence and electron density for 775 nm although it saturates at very high pump power. The linear dependence confirms a one-photon absorption mechanism, which must excite carriers from midgap states. As expected, the conversion of red photons to electrons is quite inefficient but comparable carrier densities to those from blue excitation can be obtained by using about five times higher pump power. Excitation with 387 and 400 nm photons exhibits a dependence on fluence which contains both linear and quadratic components. The additional quadratic component is attributed to TPA, which is consistent with Fig. 1(b) where blue excitation showed increasing fraction absorbed with higher excitation power.

Figure 9(a) shows the change in THz transmission upon 400 nm photoexcitation at 10 K for different pump fluences. As expected, higher pump fluence results in larger decrease in transmission due to the increased number of carriers generated by both OPA and TPA. Normalizing by the maximum

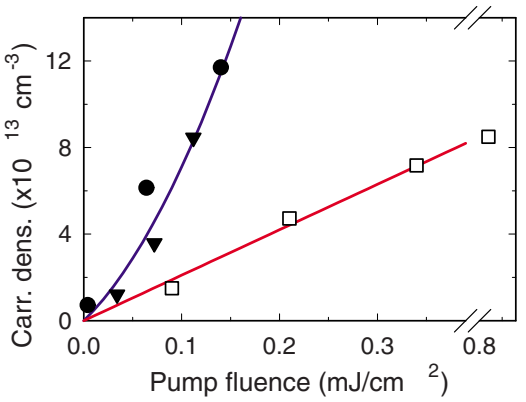

FIG. 8. (Color online) Dependence of electron density on excitation fluence with 387 nm (solid circles), 400 nm (solid triangles), and 775 nm (open squares) photons. Lines are linear (red) and quadratic (blue) fits to the data. Densities were measured 20 ps after photoexcitation, and ZnO temperature was 25 K.

transmission change as shown in Fig. 9(b), it is clear that recombination dynamics are faster when the sample is photoexcited more strongly. The primary cause of this behavior is similar to that of faster recombination dynamics at higher temperature, namely, that more carriers are present to interact with by scattering and recombination.

Different combinations of temperature and pump fluence can have similar effects on carrier dynamics. Figure 9(c) compares the photoconductivity decay at low temperature and high fluence (10 K, 0.18 mJ/cm^2) to decays for two moderate temperatures at moderate power that bracket it (50 and 60 K, 0.07 mJ/cm^2). Increasing fluence from 0.07 to 0.18 mJ/cm^2 results in an increase from $\sim 5\times10^{13}$ to $\sim 1.5\times10^{14}$ photoexcited carriers per cm^3 according to Fig. 8. The additional photogenerated carriers cause faster recombination in the same manner that is seen with thermally generated carriers, Fig. 7(b). Increasing the temperature from 10 to 55 K would introduce $\sim 1.5\times10^{15}$ electrons per cm^3 into the conduction band,[19] about an order of magnitude larger than the number of photoexcited carriers needed to produce a similar effect.

It may seem that fewer thermally generated carriers should be needed than photogenerated carriers to create the same effect on dynamics since there is also increased phonon interaction at high temperatures. However, Kane has shown for GaAs that scattering between carriers with large excess energies above the conduction band is stronger than scattering between hot carriers and a cool background plasma.[32] We see that the same effect is active in ZnO, requiring higher densities of thermally generated cool electrons to cause the same dynamics as a lower density of photoexcited hot carriers.

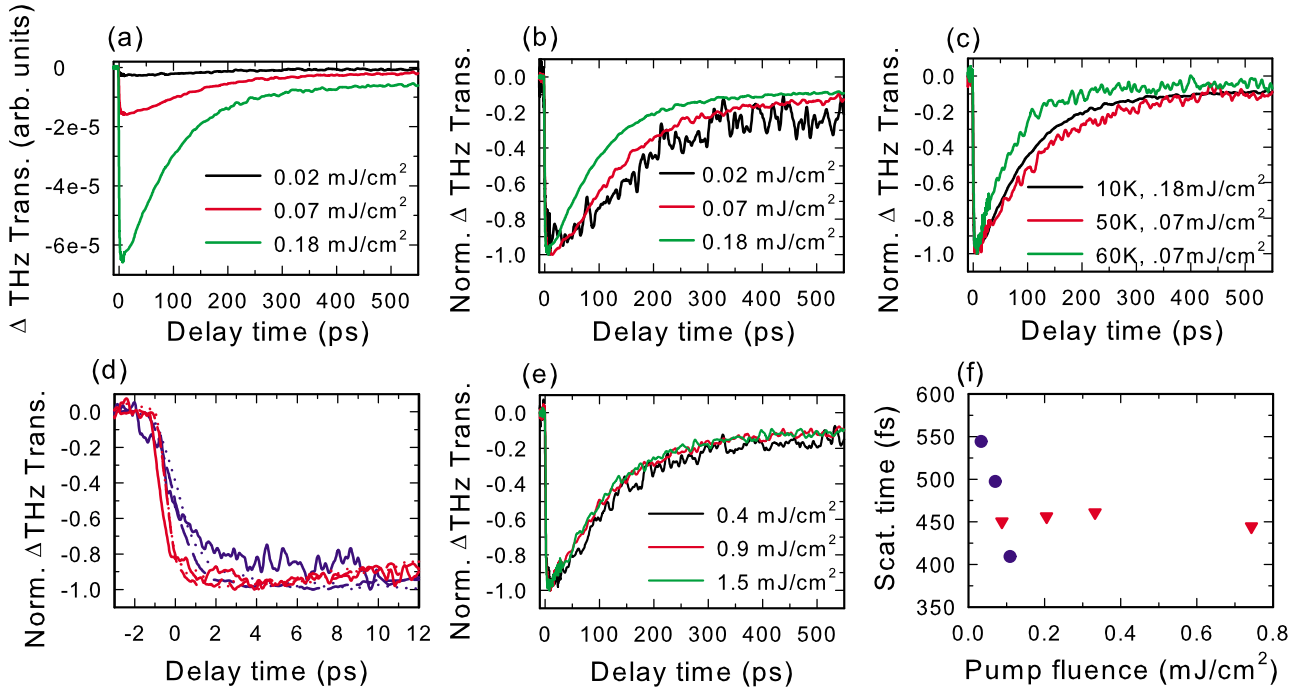

FIG. 9. (Color online) (a) Pump scans with 400 nm photoexcitation as a function of pump fluence at ZnO temperature of 10 K. (b) Normalized pump scans demonstrating faster photoconductivity decay at higher pump fluence due to higher electron density. (c) Normalized photoconductivity decay with 0.18 mJ/cm^2 excitation at 10 K ZnO temperature bracketed by two higher temperature scans (50 and 60 K) using lower power of 0.07 mJ/cm^2. (d) Pump scans at early delay time showing faster increase in photoconductivity for 775 nm excitation (red lines) than for 400 nm (blue lines) for a range of pump fluences. Excitation fluences are 0.02, 0.07, and 0.18 mJ/cm^2 for blue and 0.4, 0.9, and 1.5 mJ/cm^2 for red for solid, dotted, and dashed lines, respectively. (e) Normalized pump scans with 775 nm excitation for three different fluences, demonstrating that dynamics are independent of fluence with red excitation in this regime. (f) Scattering time as a function of pump fluence with either 400 nm (circles) or 775 nm (triangles) photons. Temperature was 25 K in both cases with delay time of 50 ps for blue and 20 ps for red.

Photoexcitation with 775 nm light also shows fast injection dynamics followed by decay in photoconductivity over hundreds of picoseconds. However, dynamics are different from blue photoexcitation in several ways. First, injection with 775 nm excitation takes place more rapidly than with 400 nm excitation as shown in Fig. 9(d). Red photoexcitation results in subpicosecond injection with time scale independent of power while injection with blue photoexcitation takes 2–4 picoseconds and is faster at higher power. Second, decay dynamics in photoconductivity after red excitation are independent of excitation fluence for the regime measured. Figure 9(e) shows the normalized pump scans for three different excitation fluences are essentially identical, in contrast to blue excitation which shows faster decay with higher pump power, Fig. 9(b). Finally, ambipolar scattering time is independent of pump fluence with 775 nm excitation but decreases with increasing pump fluence with 400 nm excitation, as shown in Fig. 9(f). These scattering times are fits of frequency-dependent complex photoconductivity at delay times of 20 ps for red excitation and 50 ps for blue. The ZnO temperature was 25 K, where interaction among photogenerated carriers plays an important role in dynamics. TPA does not occur for 775 nm excitation; and the low optical absorption indicates that electrons are being excited sparsely and nearly uniformly from shallow or midgap donor states throughout the wafer thickness by OPA. Conversely, TPA with blue photons produces light holes as well as mobile electrons, leading to higher initial ambipolar mobilities. Higher fluence of blue photons produces higher carrier densities, resulting in faster scattering into the heavy-hole band and lower mobility after 50 ps delay times.

IV. CONCLUSIONS

Carrier dynamics in photoexcited bulk ZnO have been investigated using time-resolved THz spectroscopy. The frequency-dependent photoconductivity is described well by the Drude model, which was used to extract the plasma frequency and scattering time. Photoconductivity reaches a maximum within the first ~5 ps of photoexcitation and then decays over longer time scales as carriers become trapped or recombine. Additionally, mobility decreases as light holes created by TPA cool and populate the heavy-hole band due to scattering from phonons and other carriers. The dynamics of decay depend sensitively on both the lattice temperature and the carrier density with photoconductivity decreasing over tens of picoseconds at 80 K and hundreds of picoseconds at 10 K due to both phonon density and thermally generated carriers. Higher laser fluence also generates higher carrier density, resulting in faster decay dynamics. This detailed knowledge of electron and hole dynamics, obtained with TRTS, is critical to potential application of ZnO in transparent conducting oxides, nanostructured solar cells, and light emitters.

ACKNOWLEDGMENTS

Acknowledgment is made to the Donors of the American Chemical Society Petroleum Research Fund for partial support of this research. C.A.S. acknowledges the National Science Foundation (Grant No. CHE-0616875) for partial support of this work. We also thank Jonathan Spanier and Sohrab Ismail-Beigi for helpful conversations.

*Corresponding author.
†jbaxter@drexel.edu
‡charles.schmuttenmaer@yale.edu

[1] D. M. Bagnall, Y. F. Chen, Z. Zhu, T. Yao, S. Koyama, M. Y. Shen, and T. Goto, Appl. Phys. Lett. **70**, 2230 (1997).
[2] U. Ozgur, Y. I. Alivov, C. Liu, A. Teke, M. A. Reshchikov, S. Dogan, V. Avrutin, S. J. Cho, and H. Morkoc, J. Appl. Phys. **98**, 041301 (2005).
[3] T. Minami, Semicond. Sci. Technol. **20**, S35 (2005).
[4] R. L. Hoffman, B. J. Norris, and J. F. Wager, Appl. Phys. Lett. **82**, 733 (2003).
[5] J. B. Baxter and E. S. Aydil, Appl. Phys. Lett. **86**, 053114 (2005).
[6] M. Law, L. E. Greene, J. C. Johnson, R. Saykally, and P. D. Yang, Nature Mater. **4**, 455 (2005).
[7] D. C. Olson, J. Piris, R. T. Collins, S. E. Shaheen, and D. S. Ginley, Thin Solid Films **496**, 26 (2006).
[8] E. Hendry, M. Koeberg, and M. Bonn, Phys. Rev. B **76**, 045214 (2007).
[9] D. C. Look, D. C. Reynolds, J. R. Sizelove, R. L. Jones, C. W. Litton, G. Cantwell, and W. C. Harsch, Solid State Commun. **105**, 399 (1998).
[10] K. Zitouni, A. Kadri, P. Lefebvre, and B. Gil, Superlattices Microstruct. **39**, 91 (2006).
[11] M. C. Beard, G. M. Turner, and C. A. Schmuttenmaer, Phys. Rev. B **62**, 15764 (2000).
[12] M. C. Beard, G. M. Turner, and C. A. Schmuttenmaer, J. Appl. Phys. **90**, 5915 (2001).
[13] J. B. Baxter and C. A. Schmuttenmaer, J. Phys. Chem. B **110**, 25229 (2006).
[14] M. Schall and P. U. Jepsen, Appl. Phys. Lett. **80**, 4771 (2002).
[15] S. K. E. Merchant, J. Lloyd-Hughes, L. Sirbu, I. M. Tiginyanu, P. Parkinson, L. M. Herz, and M. B. Johnston, Nanotechnology **19**, 395704 (2008).
[16] D. G. Cooke, F. A. Hegmann, Y. I. Mazur, Z. M. Wang, W. Black, H. Wen, G. J. Salamo, T. D. Mishima, G. D. Lian, and M. B. Johnson, J. Appl. Phys. **103**, 023710 (2008).
[17] P. Parkinson, J. Lloyd-Hughes, Q. Gao, H. H. Tan, C. Jagadish, M. B. Johnston, and L. M. Herz, Nano Lett. **7**, 2162 (2007).
[18] M. Walther, D. G. Cooke, C. Sherstan, M. Hajar, M. R. Freeman, and F. A. Hegmann, Phys. Rev. B **76**, 125408 (2007).
[19] J. B. Baxter and C. A. Schmuttenmaer, preceding paper, Phys. Rev. B **80**, 235205 (2009).
[20] J. B. Baxter and C. A. Schmuttenmaer, in *Terahertz Spectroscopy: Principles and Applications*, edited by S. L. Dexheimer (CRC, New York, 2008), p. 73.
[21] D. G. Thomas, J. Phys. Chem. Solids **15**, 86 (1960).
[22] N. W. Ashcroft and N. D. Mermin, *Solid State Physics* (Thomson

Learning, Inc., USA, 1976).
[23] L. E. Brus, J. Chem. Phys. **80**, 4403 (1984).
[24] W. R. L. Lambrecht, A. V. Rodina, S. Limpijumnong, B. Segall, and B. K. Meyer, Phys. Rev. B **65**, 075207 (2002).
[25] F. Bertazzi, M. Goano, and E. Bellotti, J. Electron. Mater. **36**, 857 (2007).
[26] J. R. Chelikowsky, Solid State Commun. **22**, 351 (1977).
[27] A. Kobayashi, O. F. Sankey, S. M. Volz, and J. D. Dow, Phys. Rev. B **28**, 935 (1983).
[28] *II-IV and I-VII Compounds; Semimagnetic Compounds*, edited by U. Rössler (Springer-Verlag, Berlin, 1999).
[29] M. R. Wagner, H. W. Kunert, A. G. J. Machatine, A. Hoffmann, P. Niyongabo, J. Malherbe, and J. Barnas, Microelectron. J. **40**, 289 (2009).
[30] G. F. Koster, J. O. Dimmock, R. G. Wheeler, and H. Statz, *Properties of the Thirty-Two Point Groups* (MIT, Cambridge, MA, 1963).
[31] J. Wrzesinski and D. Frohlich, Phys. Rev. B **56**, 13087 (1997).
[32] M. G. Kane, K. W. Sun, and S. A. Lyon, Phys. Rev. B **50**, 7428 (1994).